Journal of proteome research

pubs.acs.org/jpr

Article

Interactomes of Glycogen Synthase Kinase-3 Isoforms

Kevin W. Cormier, Brett Larsen, Anne-Claude Gingras, and James R. Woodgett*

Cite This: *J. Proteome Res.* 2023, 22, 977−989

Read Online

ACCESS | Metrics & More | Article Recommendations | Supporting Information

ABSTRACT: Functional differentiation of the two isoforms of the protein-serine/threonine kinase, glycogen synthase kinase-3 (GSK-3), is an unsettled area of research. The isoforms are highly similar in structure and are largely redundant, though there is also evidence for specific roles. Identification of isoform-specific protein interactors may elucidate the differences in function and provide insight into isoform-selective regulation. We therefore sought to identify novel GSK-3 interaction partners and to examine differences in the interactomes of the two isoforms using both affinity purification and proximity-dependent biotinylation (BioID) mass spectrometry methods. While the interactomes of the two isomers are highly similar in HEK293 cells, BioID in HeLa cells yielded a variety of preys that are preferentially associated with one of the two isoforms. DCP1B, which favored GSK-3α, and MISP, which favored GSK-3β, were evaluated for reciprocal interactions. The differences in interactions between isoforms may help in understanding the distinct functions and regulation of the two isoforms as well as offer avenues for the development of isoform-specific strategies.

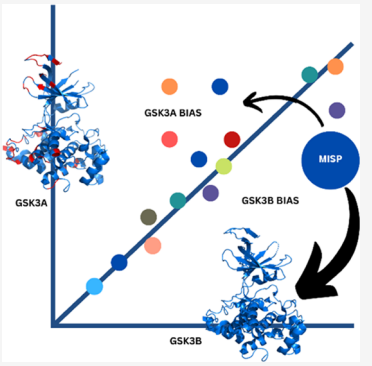

KEYWORDS: *glycogen synthase kinase-3, GSK-3, BioID, protein isoforms, interactomes, protein−protein interactions*

INTRODUCTION

Glycogen synthase kinase-3 (GSK-3) is a ubiquitously expressed and constitutively active serine/threonine kinase. The kinase is highly conserved across species, with two protein isoforms encoded by distinct genes in mammals, GSK-3α and GSK-3β. In humans, GSK3A is located on chromosome 19, while GSK3B is on chromosome 3. GSK-3α harbors a glycine-rich N-terminal extension that adds 4 kDa over the mass of GSK-3β, and in the last 76 C-terminal residues, the two proteins share only 36% identity (Figure S1). While GSK-3β has been reported to have a nuclear localization sequence,[1] the N-terminal extension of GSK-3α is implicated in nuclear exclusion.[2] The two isoforms, however, are essentially identical within their kinase domains. The evolutionary split between the isoforms arose from a common ancestor approximately at the time of vertebrate emergence possibly as part of a whole genome duplication event important for more complex species. While both isoforms are conserved in fish, amphibians, reptiles, and mammals, GSK-3α is absent in birds.[3] Gene sequence conservation between avian and mammalian GSK-3β, however, remains very high.

That birds naturally lack GSK-3α might suggest that GSK-3β is fully competent to provide GSK-3 functions and GSK-3α is merely a redundant form. Indeed, most published studies focus on the β-isoform, though for inhibitor studies, this may be misleading given that most small molecular antagonists show similar potency toward both isoforms. Despite the high degree of structural similarity, there are, however, substantial functional differences between the two isoforms. Ablation of GSK-3β in mice causes early death due to either massive liver degeneration or patterning defects in the heart,[4,5] whereas GSK-3α-null mice are viable.[6] However, subsequent to birth, GSK-3α null animals also exhibit several clear phenotypes indicating nonredundancy.[7] Inactivation of *Gsk3a* significantly reduces mouse sperm motility leading to minimal fertility.[8,9] Additionally, GSK-3α global knockout mice have been observed to have a shorter life span than their wild-type littermates.[10] This observation led to the discovery that GSK-3α is a suppressor of aging, slowing age-related pathologies in the heart, liver, small intestine, bones, and joints and suggesting that GSK-3α may have a distinct role in autophagy. GSK-3α also plays a differential role compared to the β-isoform in brain plasticity, preserving the correct balance between long-term depression (LTD) and long-term potentiation (LTP) in mouse brain[11] and GSK-3α is required for LTD through transient anchoring in dendritic spines[12] and for limiting LTP.[13]

The lethality of *Gsk3b* global knockout mice precludes determination of isoform-specific roles in knockout animal models. Conversely, genetic knockdown and knockout of GSK-3 in cell lines have offered insight into isoform-specific roles. While each GSK-3 isoform was observed to be nonessential in hundreds of human cell lines through CRISPR/Cas9 screening[14] (https://depmap.org/portal/gene/GSK3A?tab=overview)—the one exception being GSK3B in

Received: December 15, 2022
Published: February 13, 2023

the JVE-127 colorectal cancer line (https://depmap.org/portal/gene/GSK3B?tab=overview)—genetic knockout approaches have the drawback of also eliminating possible noncatalytic functions and do not account for adaptive rewiring of genetically modified cells, especially prevalent in cancer cell lines. A chemical-genetic approach has been used to study GSK-3 isoform functional differences.[15] In this case, inhibitor analogues that recognize a genetic mutation in the protein of interest were used to distinguish between highly homologous proteins. Small-molecule inhibitors that demonstrate a degree of isoform specificity have also been developed to tease apart the differences between the two GSK-3 proteins[12,16] and have, for example, implicated GSK-3α in fragile X syndrome.[17]

Despite the strong evidence for functional differences between the isoforms, there is a lack of insight into the mechanisms by which such differences are manifested. Here, we have taken an unbiased, protein-level approach to identify interactors of GSK-3 in an isoform-specific manner. A mutant *Escherichia coli* biotin ligase enzyme (BirA*) fused to GSK-3 protein stably expressed in either HEK293 Flp-In T-REx or HeLa Flp-In T-REx cells was used to biotinylate amine groups of proximal proteins that were then affinity-purified using streptavidin resin and identified using mass spectrometry (MS).[18] This proximity-dependent biotinylation (BioID) technique, together with conventional affinity purification MS (AP-MS), was used to identify potential interacting partners of GSK-3α and GSK-3β. While many interactors were shared evenly between the isoforms as expected, this analysis also revealed proteins that exhibited differential association.

EXPERIMENTAL PROCEDURES

Generation of Stable Inducible Cell Pools and BioID Labeling

Cell lines were generated in HEK293 Flp-In T-REx 293 (Invitrogen; used for BioID, affinity purification coupled to MS and some of the streptavidin-immunobot analyses) or HeLa Flp-In T-REx cells (used for BioID and the BioID-immunoblot analyses) grown at 37 °C in Dulbecco's modified Eagle's medium (DMEM) high-glucose supplemented with 10% fetal bovine serum (growth media). The parental cell lines are routinely monitored for mycoplasma contamination. For generation of stable cell lines, Flp-In T-REx cells were transfected using the jetPRIME transfection reagent (Polyplus Cat# CA89129-924). The cells were seeded at 250,000 cells/well in a six-well plate in 2 mL of growth media. The next day (day 1), the cells were transfected with 200 ng of pcDNA5-FLAG-BirA* bait construct and 2 μg of pOG44 in 200 μL of jetPRIME buffer mixed with 3 mL of jetPrime reagent (of this mix, 200 μL was added to the cells as per the manufacturer's protocol). On day 2, transfected cells were passaged to 10 cm plates, and on day 3, selected for by the addition of hygromycin to the growth media to a final concentration of 200 μg/mL. This selection media was changed every 2−3 days until clear visible colonies were present, at which point cells were scaled up to 150 mm plates. The cells were grown to 70% confluence before induction of protein expression using 1 μg/mL tetracycline, and media supplementation with 50 μM biotin for protein labeling (unless otherwise indicated). The cells were harvested 24 h later as follows: cell medium was decanted, the cells were washed once with 5 mL of phosphate-buffered saline (PBS) per 150 mm plate, and then harvested by scraping in 1 mL of ice-cold PBS. The cells from two 150 mm plates were pelleted at 500*g* for 5 min, the PBS was aspirated, and pellets were frozen on dry ice. Cell pellets were stored at −80 °C until processing. For assessing the expression levels of BirA*-FLAG tagged proteins in relation to their endogenous counterparts, expression of bait proteins was induced for 24 h as above. Cell pellets were lysed in lysis buffer (50 mM Tris−HCl pH 7.5, 150 mM NaCl, 1 mM ethylene glycol-bis(β-aminoethyl ether)-*N*,*N*,*N*′,*N*′-tetraacetic acid (EGTA), 1.5 mM $MgCl_2$, 0.4% sodium dodecyl sulfate (SDS), 1% NP-40, Sigma-Aldrich protease inhibitors P8340 1:500) and cleared lysates were analyzed by SDS-polyacrylamide gel electrophoresis (PAGE) and immunoblotting. Blots were probed for GSK-3 (1:1000, Millipore 4G-1E), FLAG M2 (1:1000, Sigma F3165), and β-tubulin (1:2000, Abcam ab6046). Fluorescent secondary antibody for mouse (800CW, LICOR 926-32210) and rabbit (680RD, LICOR 926-68071) were used at 1:5000. Blots were imaged on an Odyssey scanner (LICOR).

BioID

Cells were grown to ∼75% confluency, and bait expression and biotin labeling were induced simultaneously (1 μg/mL tetracycline, 50 μM biotin). After 24 h, the cells were rinsed and scraped into 1 mL of PBS. The cells were collected by centrifugation (500*g* for 5 min) and stored at −80 °C until further processing. Cell pellets were thawed on ice, and a 4:1 (v/w) ratio of ice-cold lysis buffer was added (50 mM Tris−HCl, pH 7.5, 150 mM NaCl, 1% Nonidet P-40 substitute, 0.4% SDS, 1.5 mM $MgCl_2$, 1 mM EGTA, benzonase, protease inhibitors). Cells were resuspended with a P1000 pipette tip (∼10−15 aspirations) and subjected to a rapid freeze/thaw cycle (dry ice to 37 °C water bath). Lysates were rotated at 4 °C for 30 min and then centrifuged at 16,000*g* for 20 min at 4 °C. Supernatants were collected and incubated with 20 μL (packed beads) of prewashed streptavidin−Sepharose 6 (GE) with rotation overnight at 4 °C. Beads were collected (500*g* for 2 min), the supernatant was discarded, and the beads were transferred to new tubes in 500 μL of lysis buffer. The beads were washed once with SDS wash buffer (50 mM Tris−HCl, pH 7.5, 2% SDS), two times with lysis buffer, and three times with 50 mM ammonium bicarbonate, pH 8.0 (ABC; all wash volumes are 500 μL with centrifugation at 500*g* for 30 s between each wash). Beads were resuspended in 100 μL of ABC containing 1 μg of sequencing-grade trypsin and gently mixed at 37 °C for 4 h. Fresh trypsin (1 μg) was added, and the samples were allowed to digest overnight. Supernatant was collected (by centrifugation at 500*g* for 2 min), and the beads were washed with 100 μL of molecular biology-grade H_2O and pooled with peptides. Digestion was terminated by acidification with formic acid (2% final concentration), and peptides were dried by vacuum centrifugation.

FLAG Affinity Purification

The FLAG AP-MS protocol was adapted from Lambert et al.[19] with slight modifications. For FLAG affinity purification, pellets from two 150 mm plates were lysed by passive lysis assisted by freeze−thaw cycles. Briefly, to the frozen cell pellet, a 1:4 pellet weight/volume ratio of ice-cold lysis buffer was added and the frozen pellet was resuspended by pipetting up and down. Lysis buffer was 50 mM *N*-(2-hydroxyethyl)-piperazine-*N*′-ethanesulfonic acid (Hepes)−NaOH pH 8.0, 100 mM KCl, 2 mM EDTA, 0.1% NP-40, 10% glycerol, 1 mM phenylmethylsulfonyl fluoride (PMSF), 1 mM dithiothreitol (DTT), and Sigma-Aldrich protease inhibitor cocktail, P8340,

https://doi.org/10.1021/acs.jproteome.2c00825
J. Proteome Res. 2023, 22, 977−989

1:500. Tubes were frozen and thawed once by putting on dry ice ca. 5−10 min and then transferring in a 37 °C water bath with agitation until only a small amount of ice remained. Thawed samples were then put on ice. The tubes were centrifuged at 16,000 rpm for 20 min at 4 °C, and the supernatant was transferred to fresh tubes. During centrifugation, anti-FLAG M2 magnetic beads (Sigma-Aldrich, M8823) were prepared: 25 μL of 50% slurry was aliquoted for each IP (2 × 150 mm^2 plates), and the beads were washed in batch mode by 3 × 1 mL of lysis buffer. To the rest of the lysate, the equivalent of 12.5 μL packed FLAG M2 magnetic beads was added and the mixture was incubated for 2 h at 4 °C with gentle agitation (nutator). The beads were pelleted by centrifugation (1000 rpm for 1 min). Most of the supernatant was removed with a pipette, and the beads were transferred with ∼200 μL of lysis buffer to a fresh tube and magnetized for ∼30 s. Residual buffer was aspirated. One wash with 1 mL of lysis buffer and two washes with 1 mL of 20 mM Tris−HCl (pH 8.0) and 2 mM $CaCl_2$ were performed. Briefly, for each of these quick washes, the sample was demagnetized, resuspended by about four up and down pipetting steps in the wash buffer, remagnetized for ∼30 s, and the supernatant was aspirated (each wash cycle takes between 1 and 2 min). After the last wash, most of the liquid was removed, followed by a brief centrifugation (1000 rpm for 1 min), prior to the removal of the last drops of liquid with a fine pipette. The now-dried beads removed from the magnet were resuspended in 5 μL of 20 mM Tris−HCl (pH 8.0). Trypsin (1 μg, Sigma-Aldrich Trypsin Singles, T7575; resuspended at 200 ng/μL in Tris buffer) was added, and the mixture was incubated at 37 °C with agitation for 4 h. After this first incubation, the sample was magnetized and the supernatant was transferred to a fresh tube. Another 500 ng of trypsin was added, and the resulting sample was incubated at 37 °C overnight (no agitation required). The next morning, formic acid was added to the sample to a final concentration of 2% (from 50% stock solution). The samples were frozen until analysis by mass spectrometry.

Mass Spectrometry Acquisition in Data-Dependent Acquisition Mode

Affinity-purified or BioID digested material from two 150 mm plates was resuspended in 12 μL of 5% formic acid and centrifuged at 16,100*g* for 1 min before 5 μL was injected by autosampler to a homemade high-performance liquid chromatography (HPLC) column (75 μm ID, 360 μm OD with spray tip generated using a laser puller) loaded with 10−12 cm of C18 reversed-phase material (ReproSil-Pur 120 C18-AQ 3 mm). The column was placed in line with an LTQ-Orbitrap Elite (Thermo Fisher Scientific) equipped with a nanoelectrospray ion source connected in line to a NanoLC-Ultra 2D plus HPLC system (Eksigent, Dublin). The LTQ-Orbitrap Elite instrument under Xcalibur 2.0 was operated in the data-dependent acquisition mode to automatically switch between one MS1 survey scan and up to 10 MS2 scans. MS1 scans at 60k res with 1 × 10^6 target and MS2 used CID fragmentation and detection in ion trap with 3 × 10^4 target. Dynamic exclusion of 15 s. Buffer A is 99.9% H_2O, 0.1% formic acid; buffer B is 99.9% acetonitrile, 0.1% formic acid. Peptides eluted over 90 min from 2 to 35% acetonitrile with a flow rate of 200 nL/min.

MS Data Analysis (Data-Dependent Acquisition)

All Thermo RAW files were saved in our local interaction proteomics LIMS, ProHits.[20] mzXML files were generated from ThermoFinnigan RAW files using the ProteoWizard[21] converter, implemented within ProHits (−filter "peakPicking true2"−filter "msLevel2"). The searched database contained the human and adenovirus complements of the RefSeq protein database (version 57) supplemented with "common contaminants" from the Max Planck Institute (http://141.61.102.106:8080/share.cgi?ssid=0f2gfuB) and the Global Proteome Machine (GPM; http://www.thegpm.org/crap/index.html) as well as sequences from common fusion proteins and epitope tags. The sequence database consisted of forward and reversed sequences; in total, 72,226 sequences were searched. The search engines were Mascot and Comet, with trypsin specificity and two missed cleavage sites allowed. Methionine oxidation and asparagine/glutamine deamidation were set as variable modifications. The fragment mass tolerance was 0.6 Da, and the mass window for the precursor was ±12 ppm. The resulting Comet and Mascot search results were individually processed by PeptideProphet,[22] and peptides were assembled into proteins using parsimony rules first described in ProteinProphet[23] into a final iProphet[24] protein output using the Trans-Proteomic Pipeline (TPP; Linux version, v0.0 Development trunk rev 0, Build 201303061711). TPP options were as follows: general options were -p0.05 -x20 -PPM -d'DECOY'; iProphet options were pPRIME and PeptideProphet options were pPAEd. All proteins with a minimal iProphet protein probability of 0.05 were parsed to the relational module of ProHits. Note that for analysis with significance analysis of interactome (SAINT), only proteins with iProphet protein probability $R \geq 0.95$ and two unique peptides are considered.

SAINT Analysis and Data Visualization

SAINTexpress (version 3.6.3)[25] was used to score proximity interactions from DDA data. SAINTexpress calculates, for each prey protein identified by a given bait, the probability of a true proximity interaction relative to negative control runs using spectral counting as a proxy for abundance. Bait runs (four biological replicates each) were compared against eight negative control runs consisting of four BirA*-FLAG-only samples and four 3xFLAG-only samples. Preys with a false discovery rate (FDR) ≤1% (Bayesian estimation based on distribution of the averaged SAINT scores across all four biological replicates) were considered high-confidence proximity interactions. Dotplots and bait vs bait (condition−condition) plots were generated using ProHits-viz[26] (prohits-viz.org). In ProHits-viz, once a prey passes the selected FDR threshold (here 1%) with at least one bait, all its quantitative values across the data set are retrieved for all baits. For dotplots, bait−prey proximity interactions falling below the 1% FDR threshold are indicated by the color of the edge. Bait vs bait plots were color-coded using a custom Perl script. Functional enrichment analysis was performed using g:Profiler using the default parameters.[27] Venn diagram was generated at www.BioVENN.nl.[28]

MaxQuant Search

MaxQuant was used to both extract raw intensities and perform label-free quantification (LFQ). Liquid chromatography−tandem mass spectrometry (LC-MS/MS) mass spectrometry RAW data files were searched against the same RefSeq human protein sequence database as above using

https://doi.org/10.1021/acs.jproteome.2c00825
J. Proteome Res. 2023, 22, 977−989

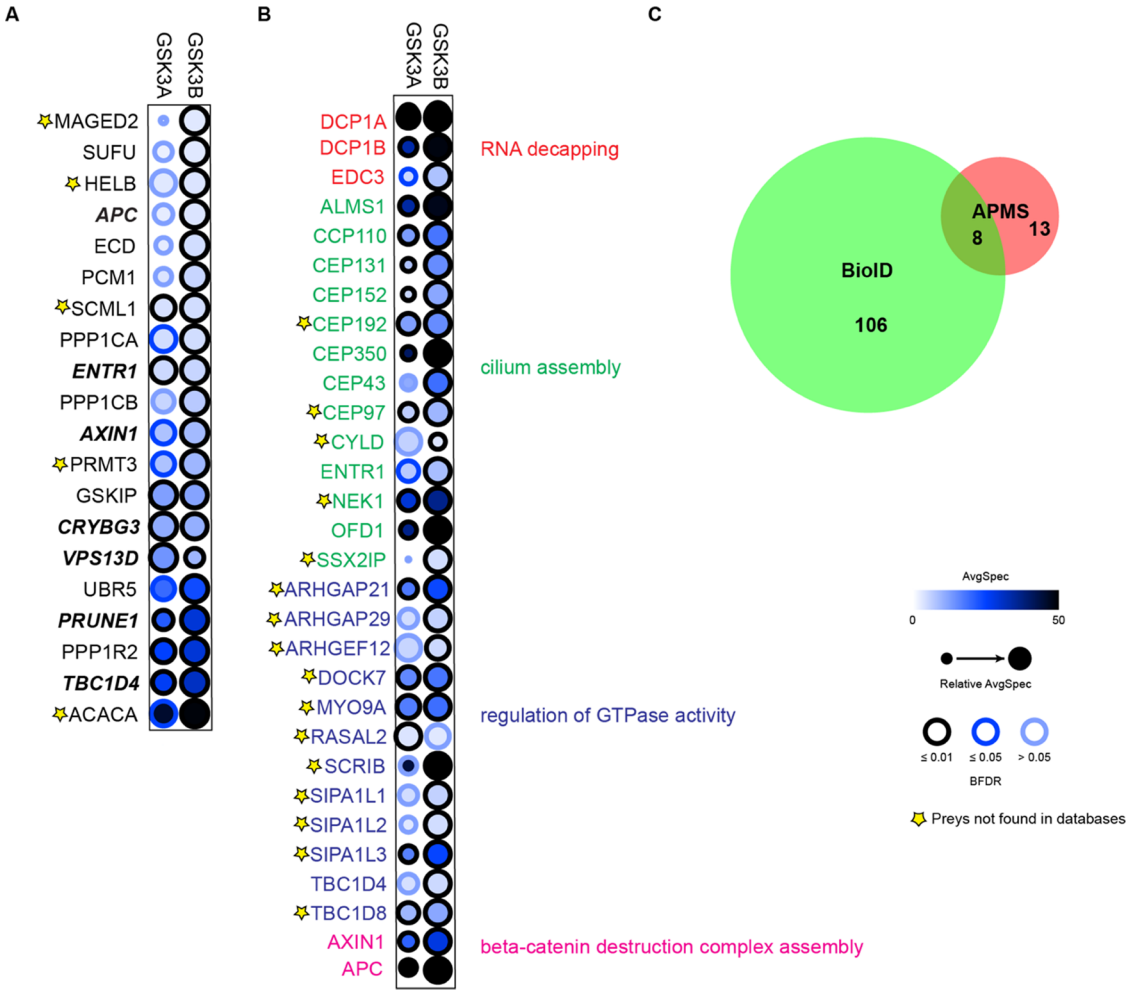

Figure 1. (A) Complete dot plot of relative average spectral counts of hits from AP-MS in HEK293 cells after SAINT filtering. Gene names that are also detected in BioID are italicized. A star indicates that the prey is not listed as an interactor of GSK-3 in BioGRID. (B) Partial dot plot of relative average spectral counts of hits from BioID in HEK293 cells after SAINT filtering. Preys are grouped and colored according to selected gene ontology (GO) terms. A star indicates that the prey is not listed as an interactor of GSK-3 in BioGRID. See Figure S3 for a complete list of 113 high-confidence interactors. (C) Venn diagram comparing AP-MS to BioID of GSK-3 in HEK293 cells. Numbers indicate those preys that passed SAINT analysis (dot plot legend as inset).

MaxQuant (v1.6.2.10).[29] For identification, the minimum peptide length was set to seven amino acids and the maximum peptide mass was set to 4600 Da. Trypsin/P digestion with a maximum of two missed cleavages was performed. Match between runs was enabled. Label-free quantification was performed with Fast LFQ with no normalization. MaxQuant searches for global proteome analysis were otherwise carried out with default settings.

Perseus Analysis

Perseus (v1.6.15.0) was used to perform statistical analysis as described previously.[30,31] MaxQuant LFQ intensities were uploaded onto the Perseus platform and $\log_2$-transformed. Rows were filtered to remove contaminants, only identified by site and reverse. The four replicates were grouped based on bait (either GSK3A or GSK3B), and rows were filtered based on a minimum of three valid values in at least one group. Histograms, unsupervised hierarchical clustering, multiscatter plots, and volcano plots were then generated using mostly default settings. The *t*-test false discovery rate (FDR) was set to 0.05, and the background variance parameter (s_0) was set to 0.1.

BioID Labeling, Streptavidin Capture, and Immunoblotting Detection

For BioID immunoblots of N-term BirA*-FLAG fusions, the respective HeLa Flp-In T-REx stable pools were incubated with tetracycline (1 μg/mL) and biotin (50 μM) for 24 h, then washed once with ice-cold PBS, harvested, and frozen at −80 °C. Cell pellets were lysed at a 4:1 lysis buffer-to-pellet ratio (v/w) (50 mM Tris pH 7.5; 150 mM NaCl; 0.4% SDS, 1% NP-40, 1.5 mM $MgCl_2$, 1 mM EGTA, benzonase nuclease 1:1000, and Sigma-Aldrich protease inhibitor cocktail, P8340, 1:500) by pipetting ∼10 times, sonicating 3 × 5 s at 50% amplitude, and then by freeze/thaw (dry ice to 37 °C). Samples were then rotated end-over-end for 30 min at 4 °C and then centrifuged for 20 min at 16,000*g* at 4 °C. Supernatants were collected and incubated with 25 μL (bead slurry) of prewashed streptavidin−Sepharose 6 (GE) with rotation overnight at 4 °C. Beads were collected (500*g* for 2 min), the supernatant was discarded, and the beads were transferred to new tubes in 500 μL of lysis buffer. Beads were washed once with SDS wash buffer (50 mM Tris−HCl, pH 7.5, 2% SDS) and twice with lysis buffer. A fraction of each protein extract (Input) was saved before the incubation with

https://doi.org/10.1021/acs.jproteome.2c00825
J. Proteome Res. 2023, 22, 977−989

Table 1. High-Confidence Interactors of GSK-3-β Identified by Liu et al.[44] and Our Study

gene	protein name	gene	protein name
AKAP11	A-kinase anchor protein 11	KIDINS220	kinase D-interacting substrate of 220 kDa
ALMS1	centrosome-associated protein ALMS1	LARP1B	La-related protein 1B
APC	adenomatous polyposis coli protein	MACF1	microtubule-actin cross-linking factor 1
ATG2B	autophagy-related protein 2 homolog B	KANK2	KN motif and ankyrin repeat domain-containing protein 2
AXIN1	axin-1	MAP7D3	MAP7 domain-containing protein 3
BAIAP2L1	brain-specific angiogenesis inhibitor 1-associated protein 2-like protein 1	NBR1	Next to BRCA1 gene 1 protein
CCDC138	coiled-coil domain-containing protein 138	OFD1	centriole and centriolar satellite protein OFD1
CEP43	centrosomal protein 43	PEX5	peroxisomal targeting signal 1 receptor
CEP131	centrosomal protein of 131 kDa	PPP3CA	serine/threonine-protein phosphatase
CEP152	centrosomal protein of 152 kDa	PPP6R1	serine/threonine-protein phosphatase 6 regulatory subunit 1
CEP350	centrosome-associated protein 350	PRUNE	exopolyphosphatase PRUNE1
CCP110	centriolar coiled-coil protein of 110 kDa	SEC16A	protein transport protein Sec16A
CRYBG3	very large A-kinase anchor protein	SPAG5	sperm-associated antigen 5
DCP1A	mRNA-decapping enzyme 1A	STON1	stonin-1
DCP1B	mRNA-decapping enzyme 1B	TRAK1	trafficking kinesin-binding protein 1
DLG5	disks large homolog 5	TRAK2	trafficking kinesin-binding protein 2
EDC3	enhancer of mRNA-decapping protein 3	VPS13D	intermembrane lipid transfer protein VPS13D
FAM193B	protein FAM193B	WDR62	WD repeat-containing protein 62

the beads. Samples (Input and IP) were prepared for SDS-PAGE by incubating for 15 min at room temperature (RT) in 2× Laemmli buffer with 5 mM biotin and then boiling for 15 min. The proteins were transferred to poly(vinylidene difluoride) (PVDF) membranes (Immobilon-FL, Millipore) and probed with antibodies to detect the FLAG-BirA* fusions and endogenous proteins: FLAG M2 (1:1000, Sigma F3165), GSK-3 (1:1000, Sigma 05-412), hPRUNE (1:1000, Sigma ABC98), MISP (1:1000, Sigma HPA049511), DCP1B (1:1000, CST13233). Blots were imaged on an Odyssey CLx (LICOR) and analyzed using Image Studio and Empiria Studio software.

RESULTS AND DISCUSSION

The distinct physiological consequences of selective deletion of the two isoforms of GSK-3 have yet to be explained at the molecular level. Given the nature of protein kinases and the very high level of similarity between the GSK-3 catalytic domains, we wished to determine whether the differences observed at the tissue and organismal level could be explained by differences in protein interactions. Indeed, it is ultimately at the level of protein−protein interactions that cellular regulation and phenotypic differences become manifest. Conversely, the phenotypic differences that have been observed in isoform-specific ablation models can only be fully understood through investigation of mechanisms that are affected by protein−protein interactions. Determination of these mechanistic differences could lead to new druggable targets for therapy. Protein−protein interaction networks that include GSK-3 have been described by several groups using different approaches.[32−36] These include yeast two-hybrid screens and affinity purification or BioID mass spec. These screens however mostly do not include both isoforms of GSK-3 and are not designed to look specifically for differences between the isoforms in the mammalian cell milieu.

The present study was designed to achieve this comparison. To compare the interactomes of the two GSK-3 isoforms, we first generated stable HEK293 cell pools that, under tetracycline induction, express a biotin ligase and 3xFLAG sequence N-terminally conjugated to the full-length sequence of GSK-3α or GSK-3β. Exposure of these cell lines to 1 μg/mL tetracycline for 24 h resulted in efficient induction of GSK-3α and GSK-3β bait expression as judged by immunoblotting (Figure S2). The BirA*-FLAG tagged GSK-3α expression level was approximately two-thirds the level of BirA*-FLAG tagged GSK-3β. By processing multiple (8−10) biological replicates for each bait and then selecting for analysis the four best replicates for each of our two baits, we gained a statistical confidence previously not attained from broader screens. We reviewed the chromatograms for all replicates of each bait, discarding any obvious outliers that had >33% decrease in total ion current (TIC) intensity from other replicate sample files. Files were also compared with respect to spectral counts for bait and streptavidin. Again outliers that had >33% difference in spectral counts were not included for analysis. Of the remaining samples, four representative replicates were chosen for further analysis. Using both AP-MS and BioID approaches, we benefitted from their complementarity to expand the GSK-3 interactome. BioID has the advantage of not only capturing weak and transient interacting partners that come into close proximity to the bait, such as a substrate, but also captures prey irrespective of the dynamic changes over the course of incubation with biotin which, in our case, was a 24 h period.

We initially used the BirA*-FLAG tagged GSK-3 (BF-GSK-3) baits for affinity purification mass spectrometry (AP-MS). Using a 1% Bayesian false discovery rate (BFDR) cutoff in SAINT[25,37] to select high-confidence proximity interactors relative to the expected spectral counts distribution observed in control samples yielded 20 high-confidence hits (Figure 1A). Twelve of these are known interactors of GSK-3, including AXIN1 and adenomatous polyposis coli (APC), which are well-characterized components of the destruction complex in the canonical Wnt signaling pathway.[38] The remaining six hits are potentially novel interactions of GSK-3 (either direct or indirect) and are not documented (searched on November 21, 2022) in PubMed, BioGRID,[39,40] or APID.[41,42] Further validation is warranted to determine whether they are true GSK-3 interactors.

As expected, BioID facilitated the detection of a broader GSK-3 proximal interactome with 113 preys identified as high-

https://doi.org/10.1021/acs.jproteome.2c00825
J. Proteome Res. 2023, 22, 977−989

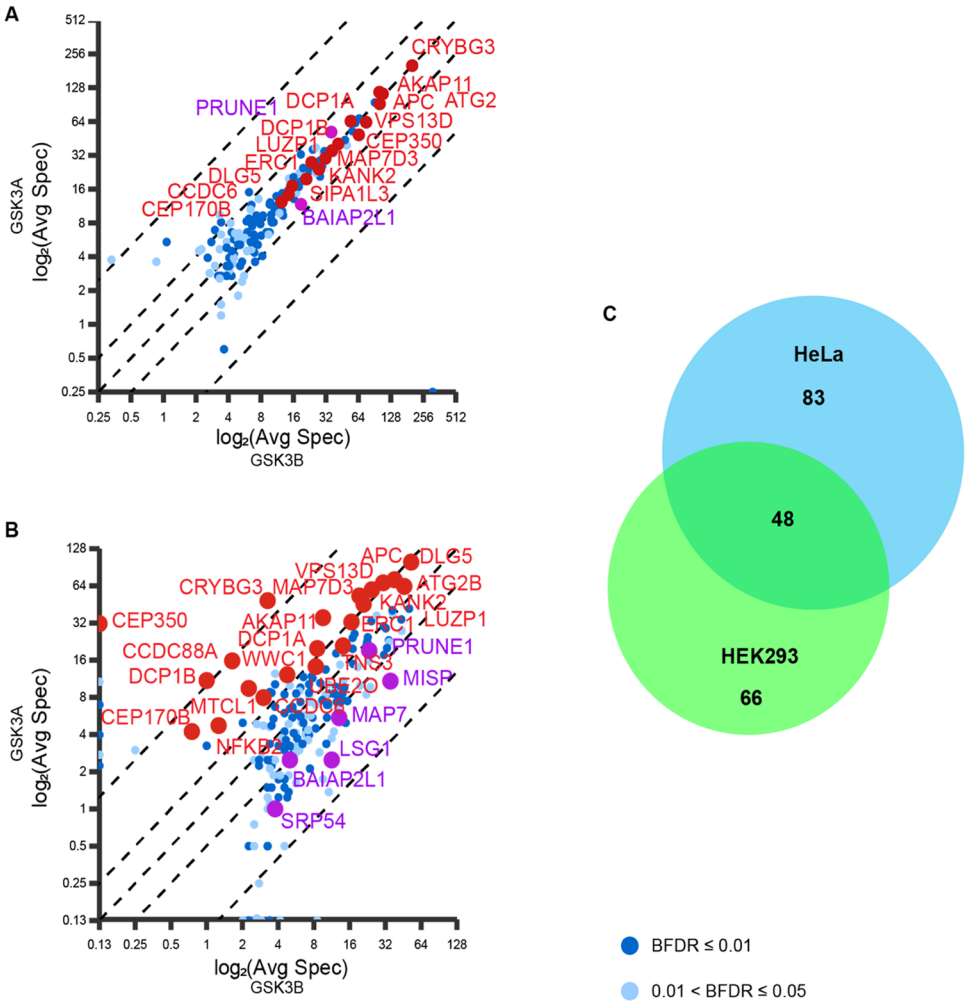

Figure 2. (A) Bait−bait plot of SAINT filtered preys from BioID in HEK293 cells. Log 2 of the average spectral counts for each bait are plotted. The 0-, 2-, and 10-fold differences are indicated by dashed lines. (B) Bait−bait plot of SAINT filtered preys from BioID in HeLa cells. Log 2 of the average spectral counts for each bait are plotted. The 0-, 2-, and 10-fold differences are indicated by dashed lines. (C) Venn diagram comparing BioID of GSK-3 in HEK293 and HeLa cells. Numbers indicate those preys that passed SAINT analysis.

confidence hits by passing our SAINT cut-offs (Figure S3). A gene ontology (GO) analysis of the BioID data supports a role for GSK-3 in a variety of biological processes. Having grouped together high-confidence hits based on biological function, we created a partial list from our dot plot of BioID in HEK293s that contain both reliable and interesting interactors (Figure 1B).

GSK-3's established role in Wnt signaling is represented by AXIN1 and APC, but there are indications of a yet unstudied role for GSK-3 in RNA decapping, cilium assembly, and regulation of GTPases. Because of the nature of AP-MS, hits from this type of experiment represent strong interactions. The BioID approach, on the other hand, is complementary to AP-MS in that it can detect "cycling" proximity interactions—those that are context-dependent and/or characterized by rapid on−off rates, and that may be present at low abundance under steady-state conditions.[43] This is enabled by the conjugated biotin ligase (BirA R118G; BirA*) activating a biotin cloud with an ∼10 nm radius that can then biotinylate surface-exposed lysines on proximal proteins. The resulting biotinylated proteins are extracted by harsh lysis, captured by streptavidin beads, and subjected to more stringent wash protocols than affinity purification allows. Besides weak and transient interactions, this method also has the advantage of detecting proteins that would otherwise remain insoluble in the cell extract pellet, as well as proteins that reside in the same cellular compartment as the bait. Eight of the interactions were identified in HEK293s by both methods (Figure 1C).

A recently published proximity-dependent biotinylation coupled to mass spectrometry study included GSK-3β as one of the baits.[44] The baits in that study were conjugated to a multiple approaches combined (MAC) tag containing both a StrepIII-tag and BirA*. There are differences between our two studies, most notably theirs involved two replicates as opposed to our four and they set a SAINT cutoff corresponding to a protein-level BFDR of 5% as opposed to our 1%. With these differences taken into consideration, they identified 57 high-confidence interactions in their BioID approach and we identified 113. Of these, 36 interactions were seen in both studies (Table 1), thereby corroborating these interactions. Despite these similarities, we nevertheless detected 67 hits that were not previously reported.

Our purpose, though, was to investigate both isoforms of GSK-3 and, when all of the SAINT filtered data are plotted as a condition−condition plot (normalized to total abundance) with each isoform bait representing a condition, the preys

https://doi.org/10.1021/acs.jproteome.2c00825
J. Proteome Res. 2023, 22, 977−989

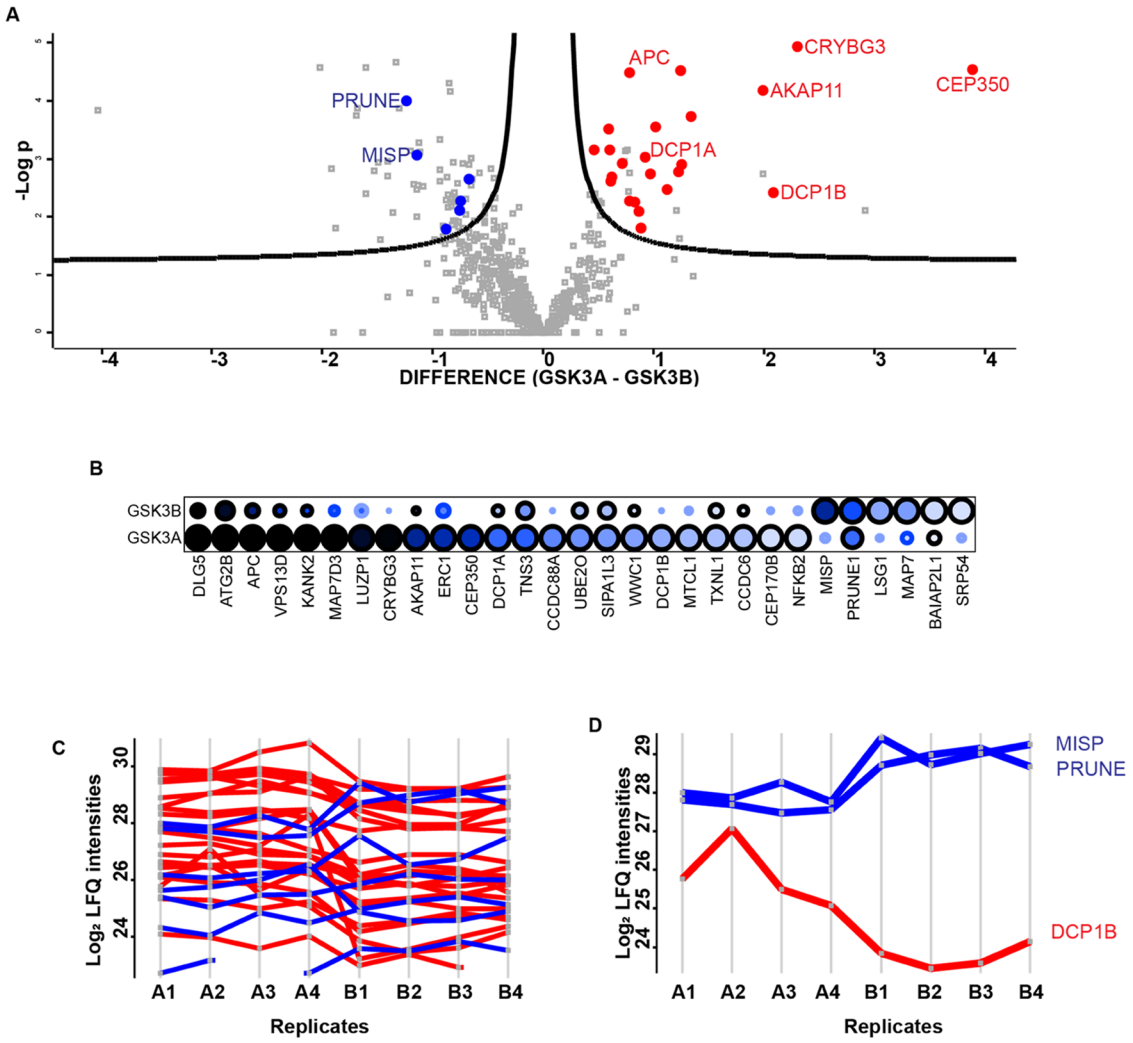

Figure 3. (A) Volcano plot of differences in LFQ intensities of preys between each GSK-3 bait from BioID in HeLa cells. Differences were calculated in Perseus, with significant difference evaluated by Student's *t*-test at 5% false discovery rate (FDR) and fold change (s_0) >0.1. (B) Dot plot of relative average spectral counts of preys from BioID in HeLa cells that have significant differences in their LFQ intensities. (C) Profile plot of LFQ intensities for replicates of BioID in HeLa for all preys with significant differences between isoforms and passed SAINT filtering by spectral counting. (D) Profile plot LFQ intensities across replicates for MISP, PRUNE, and DCP1B in HeLa cells.

mostly populate the diagonal (Figure 2A). From these data, we concluded that we could not detect any isoform-exclusive interactors and that the preys interact to an equivalent degree with each isoform over the course of the 24 h incubation period.

To confirm and expand upon these BioID results, we performed a similar experiment using stable HeLa Flp-In T-REx cells. In comparison with the HEK293 cell results, the HeLa-cell-derived data did not fall as tightly on the diagonal when visualized as a condition−condition plot (Figure 2B) nor was the distribution simply skewed in favor of GSK-3β (which may have been expected due to higher GSK-3β bait expression in the HeLa cells) since preys fell off the diagonal in both directions. Given the distribution of the data, this suggested that certain preys may show preference for a GSK-3 isoform in HeLa cells. Important to note is that some of these off-diagonal hits in HeLa cells are on-diagonal in HEK293 cells. This suggests a cell type dependency of the prey discrimination between isoforms. The results using HeLa cells further expanded our GSK-3 interactome by adding 83 preys not detected or not passing SAINT filtering in HEK293 cells, for a total of 197 high-confidence interactors of GSK-3 (Figure 2C). These additional 83 proteins include 5 proteins that are involved in the Hippo signaling pathway (DLG5, LIMD1, SCRIB, TP53BP2, and WWC1)—though DLG5 may be a HeLa specific background signal as it shows up in many HeLa experiments.

While spectral counting works well for the identification of interactors, peak intensities are preferred to accurately quantify relative protein abundance. We thus proceeded to extract peptide peak intensities for quantification using MaxQuant for our entire data set. Doing so also provided us with MaxQuant-generated label-free quantification (LFQ) intensities.[30,45] To determine whether the normalization performed by MaxQuant's calculation of LFQ intensities was appropriately applied to our data set, we performed our own normalization of the raw intensities for SAINT filtered prey using a shared peptide of GSK-3 and a second normalization using the sum of the intensities from GSK-3α and GSK-3β at the protein group level (Figure S4). Since the normalization from MaxQuant's LFQ intensities gave a similar distribution in a condition−condition plot as both of our custom normalizations, we

https://doi.org/10.1021/acs.jproteome.2c00825
J. Proteome Res. 2023, 22, 977−989

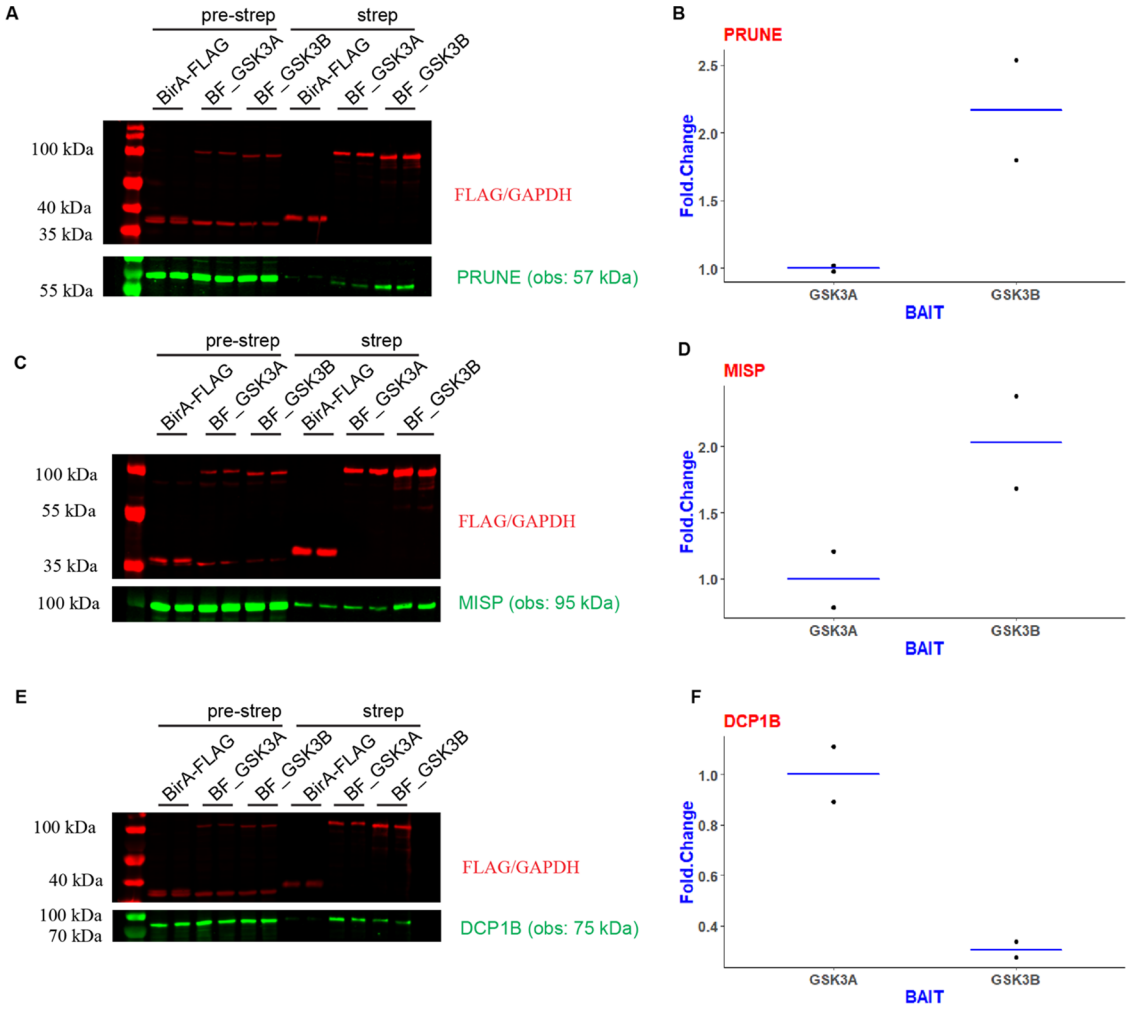

Figure 4. (A) Induction of biotinylation and streptavidin pull-down (strep) coupled to detection of the target (PRUNE) by Western blot, here referred to as BioID Western. GAPDH as loading control; FLAG blot showing levels of bait. (B) Fold change of PRUNE capture between GSK-3 isoforms as observed from BioID Westerns in HeLa cells. The horizontal line represents the mean of the two biological replicates. (C) BioID Western blot for MISP. (D) Fold change of MISP capture between GSK-3 isoforms. (E) BioID Western blot for DCP1B. (F) Fold change of DCP1B capture between GSK-3 isoforms. Note, the entire membrane for the blots is included in Figure S6.

proceeded to use the LFQ intensities generated by MaxQuant for our entire data set for further analysis.

Statistical analysis was performed to determine whether any preys were favored by one isoform by importing the LFQ intensities from MaxQuant for the four replicates of each isoform into Perseus software. Since we wanted only the replicates with GSK-3α and GSK-3β as baits to be adjusted for their respective expression levels, control baits were not included in the MaxQuant runs. Without the control samples, however, our data contained both genuine hits and background contaminants. While MaxQuant reports low intensities simply as an LFQ intensity of zero, which lends to a non-Gaussian distribution of the data as seen in the histograms, no imputation was performed to artificially adjust for low-intensity missing values. The four replicates of each isoform were grouped, and a valid value was required in three of the four replicates of at least one group to be reported. We then performed hierarchical clustering and generated volcano plots. For the volcano plot, which plots the negative logarithm of the p-value from the two sample t-test against the difference between the means of logarithmic abundances, we set the FDR to 0.05 and the background variance parameter (s_0) to 0.1. The volcano plot (Figure 3A) then represents not only the size of the difference between isoforms (x-axis) but also variance between replicates (y-axis). While there are no universal settings for FDR and s_0 that guarantee high-quality results, these thresholds were maintained between experiments to allow comparison of the HEK293 and HeLa cell data.

There were no hits that passed our significance thresholds in HEK293 cells, neither using AP-MS nor BioID methods (Figure S5). The data from BioID performed in HeLa cells, however, had 94 hits that passed our significance thresholds, with 32 favoring GSK-3α and 62 favoring GSK-3β. Because this analysis was done without filtering against control baits, we then extracted those hits which had previously passed our SAINT analysis based on spectral counting (Figure 3B). In this way, we were able to obtain a list of high-confidence hits that had quantifiable differences between GSK-3α and GSK-3β (Table S1). This yielded 29 hits, 23 of which favored GSK-3α and 6 favored GSK-3β. Importantly, the data showed good reproducibility, with low variance between replicates (Figure 3C). A number of these proteins are involved in microtubule cytoskeleton organization (GO: 0000226 and 0007010) or in

https://doi.org/10.1021/acs.jproteome.2c00825
J. Proteome Res. 2023, 22, 977−989

the establishment or maintenance of cell polarity (GO: 0007163).

To validate these mass spectrometry results, we coupled the induction of biotinylation and streptavidin pull-down to detection of the target by western blot, here referred to as BioID Western. Using a GSK-3 isoform as bait, immunoblotting was performed to detect the putative interactors (Figures 4 and S6). For these BioID Westerns, three proteins were chosen that had available, well-characterized antibodies: MISP and PRUNE that favored GSK-3β and DCP1B that favored GSK-3α in our BioID MS results. PRUNE is a well-established interactor of GSK-3β[46] and DCP1B has recently been reported in a proximity-labeled MS experiment[44] and a high-throughput two-hybrid screen,[47] while MISP is a potential novel interactor of GSK-3. The mean expression levels of BirA*-FLAG tagged bait from three replicates were determined to be 2.15 times higher for GSK-3β versus GSK-3α. This value was then used to normalize the average of the signal intensity from three replicates for each of the preys selected. MISP and PRUNE showed an approximately 4-fold increase in signal intensity in favor of GSK-3β, whereas DCP1B demonstrated a 7-fold preference of GSK-3α. These findings were in agreement with our BioID MS data.

While PRUNE is reported as interacting with GSK-3β and this is dependent on GSK-3 being active, it is not a substrate of GSK-3.[46] Though the original report of this interaction focuses on GSK-3β since they used a pan-GSK-3 antibody in their immunoprecipitation experiment, the presence of both isoforms was detected. Near-equal levels of the two isoforms of GSK-3 are detected in lysates of HeLa S3 cells, but, when immunoprecipitated by anti-h-prune antibody, there is a strong preference for GSK-3β. Our results from BioID in HeLa cells corroborate this finding. This serves not only to indicate that interactions discriminate between the two isoforms of GSK-3 but also as a proof of principle of our method.

The other two high-confidence hits that we observed to have an isoform preference are not described in the literature as substrates of GSK-3, and indeed this cannot be determined solely by BioID. Our findings, however, suggest that there is merit in the further characterization of these interactions. Both DCP1B (and its homolog, DCP1A) and MISP have multiple phosphorylation sites, and their phosphorylation has been implicated in biological function. Notably, DCP1A and DCP1B are hyper-phosphorylated during mitosis, this leading to the disassembly of the processing bodies (p-bodies).[48] In DCP1A, serine 315 has been identified as phosphorylated in interphase and important in the subsequent hyper-phosphorylation of residues in the 200−380 amino acids region. S315 had been further characterized as phosphorylated by JNK in response to IL-1 treatment[49] and then shown to also be phosphorylated by ERK, together with S319.[50] These or other kinases could act to prime DCP1A for phosphorylation by GSK-3.

While the interaction of GSK-3 and MISP is not indicated by prior protein−protein interaction studies, it too remains a potential substrate. MISP is highly phosphorylated during mitosis, with it playing a role in the transition from metaphase to anaphase and spindle positioning through regulation by Cdk1 priming and subsequent phosphorylation by Plk1.[51] Serines 471 and 541, which are highly phosphorylated in mitotic MISP,[52] are involved in the phosphorylation-dependent negative regulation of actin-binding activity. The phosphorylation of MISP is also critical in cells during interphase, with the phosphorylation of serines 394, 395, and 400 increasing its actin-bundling activity and inducing stress fiber formation.[53] These studies were largely done in vitro and the associated kinases have yet to be identified, leaving open the possibility for GSK-3 involvement in these or other functions.

The ability to use harsher detergents in the BioID method allowed for recovery of parts of the GSK-3 interactome that would otherwise have remained in the cellular debris pellet after lysis. These included several centrosomal proteins that are known to be precipitated within the pelletable matrix. We note that neither AP-MS nor BioID determines whether a detected interaction is direct or indirect. In both cases, some members of a protein complex may be more easily detected than others due to lability of bonds within the complex, proteolytic and fragmentation patterns, size, lysine frequency (for BioID), and abundance. That said, since larger proteins are more easily detected, their presence in a sample may indicate the presence of other proteins with which they form complexes. From this perspective, our identification of both centrosomal proteins and p-body proteins raises the possibility that GSK-3 interacts with the complexes that make up these organelles. Accessing data available through ProHits-web, neither of the BioID studies dedicated to the centrosome[54] or p-bodies[55] yielded GSK-3 as a high-confidence hit. When the search is widened to include lower-confidence data (i.e., in one of two biological replicates with two or three total spectral counts), GSK-3 is detected in both ciliated and nonciliated HEK293 cells. In nonciliated cells, with CNTROB, OFD1, and CEP170 as baits, GSK3A is seen in nonciliated cells; with CEP128, SASS6, CEP97, and FGFR1OP, GSK3B is seen. In ciliated cells, PCM1 as bait sees GSK3A; RPGRIP1L and CEP128 see GSK3B. Although GSK-3 appears solely as a lower-confidence hit in these screens, when GSK-3 was used as bait, as in our study, some of these same proteins are detected as high-confidence hits. The components of protein complexes can be identified by combining BioID with CRISPR/Cas9 knockout methods where the disruption of particular interactions can be used to determine the interdependency of proximity partners. The CRISPR-Cas9-mediated ablation of genes encoding individual complex subunits in pooled cell populations followed by BioID (referred to by Hesketh et al. as KO-BioID)[56] can help to elucidate whether an ablated gene affects localization or its functional connections to specific protein complexes.

GSK-3, however, does not appear to play a significant role as a scaffolding protein per se and is not a constitutive component of centrosomes or of p-bodies. Specific organelle purification methods used to determine components would also not serve to identify GSK-3's involvement. Instead, GSK-3's ubiquitous distribution in the cytoplasm means that it likely interacts with proteins prior to organelle formation or in a transient way with structural complexes (with the notable exception of the β-catenin destruction complex).

Of note, in both our AP-MS and BioID datasets, we identified Axin as an interactor of both GSK-3α and GSK-3β (Figure 1A,B). Chen et al.[15] using a chemical genetics approach to discriminate between the two isoforms concluded that GSK-3β preferentially bound to Axin when GSK-3α is chemically inhibited and that GSK-3α only bound axin when the β-isoform had been genetically knocked out. These data suggested that GSK-3β was the physiologically relevant isoform for Wnt signaling. This is difficult to reconcile with

https://doi.org/10.1021/acs.jproteome.2c00825
J. Proteome Res. 2023, 22, 977−989

our mass spectrometry data, which indicate that both isoforms show similar recovery for Axin and the destruction complex. Our data support an equivalent role for both forms of GSK-3 in the Wnt pathway.

The most puzzling finding from our study was the differences between the HEK293 and HeLa cell data. Preys identified in HeLa cells as interacting preferentially for one isoform of GSK-3 were found to be indiscriminate in our HEK293 data. Even in HeLa cells, however, it is important to note that there are no preys that are detected exclusively by one bait and that a significant majority of preys exhibit no statistically significant isoform discrimination. This suggests that GSK-3 isoform-specific associations are context-dependent.

That most preys are isoform-independent was expected since the two isoforms of GSK-3 exhibit significant functional redundancy. For example, in mammary epithelia, expression of just one allele of either GSK-3 isoform was sufficient to suppress mammary tumorigenesis.[57] Additionally, when attempts were made to quantify differences between isoforms using hits that displayed differences now as baits, we did not observe the same degree of discrimination between isoforms. Because GSK-3 isoforms are so similar structurally, we suspect that when GSK-3 interactors are exposed to both isoforms in vitro, there will be little to no difference between the interactions. Instead, differences between the degree of interaction between the two isoforms are more dependent on differences between expression levels of the isoforms and their spatial localization within intact cells.

An isoform specificity may also be cell cycle phase-dependent. Such a dependency would have been diluted from our use of BioID over a 24 h incubation period since it captures a population at different stages of the cell cycle. Cell cycle dependency could be assessed by synchronizing cells and using Turbo or miniTurbo as the biotinylation enzyme, thus allowing for shorter incubation periods.

A previously identified scaffolding protein shown to interact with GSK-3 is AKAP11.[58] In the original publication, interaction with GSK-3β, but not GSK-3α, was observed when AKAP11 was immunoprecipitated from PC12 cells.[58] While it was noted in this study that GSK-3α is expressed at low levels in these cells,[58] subsequent literature has taken this to mean that AKAP11 interacts exclusively with GSK-3β. Our AP-MS data, however, showed that AKAP11 interacts equally with both isoforms and, interestingly, our BioID data indicate that AKAP11 interacts preferentially with GSK-3α in HeLa cells. If this proves to be indeed the case, it could serve to further understand mechanistically the distinctive functional role GSK-3α plays in sperm motility in which AKAP11 has been implicated.[47,59]

As mentioned in the Introduction section, GSK-3 is evolutionarily conserved. In Drosophila, the single GSK-3 orthologue, Shaggy, is differentially spliced and distinct proteins are expressed in certain tissues with identical kinase domains but distinct N- and C-terminal domains.[60] Recently, proteins associated with two tagged proteoforms of Shaggy by AP-MS have been reported.[61] In this study, a widely expressed isoform (Sgg-PB) was compared with a neuronally restricted isoform (Sgg-PA) and the two were found to have somewhat distinct interactors. Comparing these interactomes with that of the AP-MS experiments reported here (Figure 1A) reveals little overlap of proteins for which we can identify orthologues, with the exception of β-catenin/armadillo, which is present in all four of the interactomes. Since there are up to 10 distinct splice products of Shaggy in Drosophila, it remains possible that the differentially expressed, extra-kinase domain regions may act to recruit distinct proteins, perhaps allowing for differential subcellular localization and/or access to substrates.

CONCLUSIONS

In summary, while we cannot exclude the possibility of isoform-specific protein interactors of the two mammalian isoforms of GSK-3, we conclude that the vast majority of GSK-3 interactors show no or, at most, subtle preferences and this suggests that the physiological differences between the isoforms either lies in other properties yet to be determined or are the result of consolidation of many small differences. From our data, specific isoform interactions are unlikely to account for the significant physiological differences that are observed between gene knockout models.

ASSOCIATED CONTENT

Supporting Information

The Supporting Information is available free of charge at https://pubs.acs.org/doi/10.1021/acs.jproteome.2c00825.

Sequence alignment of GSK-3 isoforms (Figure S1); Western blots of bait expression (Figure S2); complete dot plot from BioID in HEK293 cells for SAINT filtered hits (Figure S3); comparison of normalization methods of HeLa BioID data (Figure S4); volcano plots of data from AP-MS and BioID in HEK293 cells (Figure S5); and images of entire membranes for Western blots in Figure 4 (Figure S6) (PDF)

Significant hits from BioID in HeLa cells (Table S1) (XLSX)

Accession Codes

The mass spectrometry proteomics data have been deposited as a complete submission to the MassIVE repository (https://massive.ucsd.edu/ProteoSAFe/static/massive.jsp) and assigned the accession number MSV000090908. The ProteomeXchange accession is PXD038864.

AUTHOR INFORMATION

Corresponding Author

James R. Woodgett − *Lunenfeld-Tanenbaum Research Institute, Mount Sinai Hospital, Toronto, Ontario M5G 1X5, Canada; Department of Medical Biophysics, University of Toronto, Toronto, Ontario M5G 1L7, Canada;* orcid.org/0000-0003-3731-5797; Phone: 1-416-586-4800; Email: woodgett@lunenfeld.ca

Authors

Kevin W. Cormier − *Lunenfeld-Tanenbaum Research Institute, Mount Sinai Hospital, Toronto, Ontario M5G 1X5, Canada;* orcid.org/0000-0003-4070-0426

Brett Larsen − *Lunenfeld-Tanenbaum Research Institute, Mount Sinai Hospital, Toronto, Ontario M5G 1X5, Canada*

Anne-Claude Gingras − *Lunenfeld-Tanenbaum Research Institute, Mount Sinai Hospital, Toronto, Ontario M5G 1X5, Canada; Department of Molecular Genetics, University of Toronto, Toronto, Ontario M5S 1A8, Canada;* orcid.org/0000-0002-6090-4437

Complete contact information is available at: https://pubs.acs.org/10.1021/acs.jproteome.2c00825

Author Contributions

K.W.C. carried out all of the proteomic and biochemical analyses with expert technical input from B.L. K.W.C. and B.L. conducted data analysis. K.W.C. and J.R.W. conceived the project. K.W.C., J.R.W., and A.-C.G. interpreted the data and wrote the manuscript. All authors reviewed and edited the manuscript.

Notes

The authors declare no competing financial interest.

■ ACKNOWLEDGMENTS

The authors thank James Knight for the gift of BirA-FLAG tagged GSK3B cloned into HeLa Flp-In cells. This work was supported by a CIHR (Canadian Institutes of Health Research) Foundation grant (#143221) and a Terry Fox Research Institute grant to J.R.W.

■ ABBREVIATIONS

AP-MS, affinity purification mass spectrometry; BFDR, Bayesian false discovery rate; BioID, proximity-dependent biotinylation mass spectrometry; BirA*, mutant *E. coli* biotin ligase enzyme; FDR, false discovery rate; GO, gene ontology; GSK-3, glycogen synthase kinase-3; LFQ, label-free quantification; LTD, long-term depression; LTP, long-term potentiation; MAC, multiple approaches combined; MS, mass spectrometry; p bodies, processing bodies; SAINT, significance analysis of interactome

■ REFERENCES

(1) Shin, S. H.; Lee, E. J.; Chun, J.; Hyun, S.; Kim, Y. I.; Kang, S. S. The Nuclear Localization of Glycogen Synthase Kinase 3β Is Required Its Putative PY-Nuclear Localization Sequences. *Mol. Cells* **2012**, *34*, 375−382.

(2) Meares, G. P.; Jope, R. S. Resolution of the Nuclear Localization Mechanism of Glycogen Synthase Kinase-3. *J. Biol. Chem.* **2007**, *282*, 16989−17001.

(3) Alon, L. T.; Pietrokovski, S.; Barkan, S.; Avrahami, L.; Kaidanovich-Beilin, O.; Woodgett, J. R.; Barnea, A.; Eldar-Finkelman, H. Selective Loss of Glycogen Synthase Kinase-3α in Birds Reveals Distinct Roles for GSK-3 Isozymes in Tau Phosphorylation. *FEBS Lett.* **2011**, *585*, 1158−1162.

(4) Hoeflich, K. P.; Luo, J.; Rubie, E. A.; Tsao, M.-S.; Jin, O.; Woodgett, J. R. Requirement for Glycogen Synthase Kinase-3β in Cell Survival and NF-KB Activation. *Nature* **2000**, *406*, 86−90.

(5) Kerkela, R.; Kockeritz, L.; MacAulay, K.; Zhou, J.; Doble, B. W.; Beahm, C.; Greytak, S.; Woulfe, K.; Trivedi, C. M.; Woodgett, J. R.; Epstein, J. A.; Force, T.; Huggins, G. S. Deletion of GSK-3β in Mice Leads to Hypertrophic Cardiomyopathy Secondary to Cardiomyoblast Hyperproliferation. *J. Clin. Invest.* **2008**, *118*, 3609−3618.

(6) MacAulay, K.; Doble, B. W.; Patel, S.; Hansotia, T.; Sinclair, E. M.; Drucker, D. J.; Nagy, A.; Woodgett, J. R. Glycogen Synthase Kinase 3α-Specific Regulation of Murine Hepatic Glycogen Metabolism. *Cell Metab.* **2007**, *6*, 329−337.

(7) Silva-García, O.; Cortés-Vieyra, R.; Mendoza-Ambrosio, F. N.; Ramírez-Galicia, G.; Baizabal-Aguirre, V. M. GSK3α: An Important Paralog in Neurodegenerative Disorders and Cancer. *Biomolecules* **2020**, *10*, No. 1683.

(8) Aparicio, I. M.; Bragado, M. J.; Gil, M. C.; Garcia-Herreros, M.; Gonzalez-Fernandez, L.; Tapia, J. A.; Garcia-Marin, L. J. Porcine Sperm Motility Is Regulated by Serine Phosphorylation of the Glycogen Synthase Kinase-3α. *Reproduction* **2007**, *134*, 435−444.

(9) Bhattacharjee, R.; Goswami, S.; Dey, S.; Gangoda, M.; Brothag, C.; Eisa, A.; Woodgett, J.; Phiel, C.; Kline, D.; Vijayaraghavan, S. Isoform-Specific Requirement for GSK3α in Sperm for Male Fertility. *Biol. Reprod.* **2018**, *99*, 384−394.

(10) Zhou, J.; Freeman, T. A.; Ahmad, F.; Shang, X.; Mangano, E.; Gao, E.; Farber, J.; Wang, Y.; Ma, X.-L.; Woodgett, J.; Vagnozzi, R. J.; Lal, H.; Force, T. GSK-3α Is a Central Regulator of Age-Related Pathologies in Mice. *J. Clin. Invest.* **2013**, *123*, 1821−1832.

(11) Shahab, L.; Plattner, F.; Irvine, E. E.; Cummings, D. M.; Edwards, F. A. Dynamic Range of GSK3α Not GSK3β Is Essential for Bidirectional Synaptic Plasticity at Hippocampal CA3-CA1 Synapses. *Hippocampus* **2014**, *24*, 1413−1416.

(12) Draffin, J. E.; Sánchez-Castillo, C.; Fernández-Rodrigo, A.; Sánchez-Sáez, X.; Ávila, J.; Wagner, F. F.; Esteban, J. A. GSK3α, Not GSK3β, Drives Hippocampal NMDAR-Dependent LTD via Tau-Mediated Spine Anchoring. *EMBO J.* **2020**, *40*, No. e105513.

(13) Ebrahim Amini, A.; Miyata, T.; Lei, G.; Jin, F.; Rubie, E.; Bradley, C. A.; Woodgett, J. R.; Collingridge, G. L.; Georgiou, J. Specific Role for GSK3α in Limiting Long-Term Potentiation in CA1 Pyramidal Neurons of Adult Mouse Hippocampus. *Front. Mol. Neurosci.* **2022**, *15*, No. 852171.

(14) Hart, T.; Chandrashekhar, M.; Aregger, M.; Steinhart, Z.; Brown, K. R.; MacLeod, G.; Mis, M.; Zimmermann, M.; Fradet-Turcotte, A.; Sun, S.; Mero, P.; Dirks, P.; Sidhu, S.; Roth, F. P.; Rissland, O. S.; Durocher, D.; Angers, S.; Moffat, J. High-Resolution CRISPR Screens Reveal Fitness Genes and Genotype-Specific Cancer Liabilities. *Cell* **2015**, *163*, 1515−1526.

(15) Chen, X.; Wang, R.; Liu, X.; Wu, Y.; Zhou, T.; Yang, Y.; Perez, A.; Chen, Y.-C.; Hu, L.; Chadarevian, J. P.; Assadieskandar, A.; Zhang, C.; Ying, Q.-L. A Chemical-Genetic Approach Reveals the Distinct Roles of GSK3α and GSK3β in Regulating Embryonic Stem Cell Fate. *Dev. Cell* **2017**, *43*, 563.e4−576.e4.

(16) Wagner, F. F.; Benajiba, L.; Campbell, A. J.; Weïwer, M.; Sacher, J. R.; Gale, J. P.; Ross, L.; Puissant, A.; Alexe, G.; Conway, A.; Back, M.; Pikman, Y.; Galinsky, I.; DeAngelo, D. J.; Stone, R. M.; Kaya, T.; Shi, X.; Robers, M. B.; Machleidt, T.; Wilkinson, J.; et al. Exploiting an Asp-Glu "Switch" in Glycogen Synthase Kinase 3 to Design Paralog-Selective Inhibitors for Use in Acute Myeloid Leukemia. *Sci. Transl. Med.* **2018**, *10*, No. eaam8460.

(17) McCamphill, P. K.; Stoppel, L. J.; Senter, R. K.; Lewis, M. C.; Heynen, A. J.; Stoppel, D. C.; Sridhar, V.; Collins, K. A.; Shi, X.; Pan, J. Q.; Madison, J.; Cottrell, J. R.; Huber, K. M.; Scolnick, E. M.; Holson, E. B.; Wagner, F. F.; Bear, M. F. Selective Inhibition of Glycogen Synthase Kinase 3α Corrects Pathophysiology in a Mouse Model of Fragile X Syndrome. *Sci. Transl. Med.* **2020**, *12*, No. eaam8572.

(18) Roux, K. J.; Kim, D. I.; Raida, M.; Burke, B. A Promiscuous Biotin Ligase Fusion Protein Identifies Proximal and Interacting Proteins in Mammalian Cells. *J. Cell Biol.* **2012**, *196*, 801−810.

(19) Lambert, J.-P.; Tucholska, M.; Go, C.; Knight, J. D. R.; Gingras, A.-C. Proximity Biotinylation and Affinity Purification Are Complementary Approaches for the Interactome Mapping of Chromatin-Associated Protein Complexes. *J. Proteomics* **2015**, *118*, 81−94.

(20) Liu, G.; Knight, J. D. R.; Zhang, J. P.; Tsou, C.-C.; Wang, J.; Lambert, J.-P.; Larsen, B.; Tyers, M.; Raught, B.; Bandeira, N.; Nesvizhskii, A. I.; Choi, H.; Gingras, A.-C. Data Independent Acquisition Analysis in ProHits 4.0. *J. Proteomics* **2016**, *149*, 64−68.

(21) Adusumilli, R.; Mallick, P.Data Conversion with ProteoWizard MsConvert. In *Proteomics*; Comai, L., Ed.; Methods in Molecular Biology; Humana Press, 2017; Vol. *1550*, pp 339−368.

(22) Keller, A.; Nesvizhskii, A. I.; Kolker, E.; Aebersold, R. Empirical Statistical Model to Estimate the Accuracy of Peptide Identifications Made by MS/MS and Database Search. *Anal. Chem.* **2002**, *74*, 5383−5392.

(23) Nesvizhskii, A. I.; Keller, A.; Kolker, E.; Aebersold, R. A Statistical Model for Identifying Proteins by Tandem Mass Spectrometry. *Anal. Chem.* **2003**, *75*, 4646−4658.

(24) Shteynberg, D.; Deutsch, E. W.; Lam, H.; Eng, J. K.; Sun, Z.; Tasman, N.; Mendoza, L.; Moritz, R. L.; Aebersold, R.; Nesvizhskii, A. I. iProphet: Multi-Level Integrative Analysis of Shotgun Proteomic Data Improves Peptide and Protein Identification Rates and Error Estimates. *Mol. Cell. Proteomics* **2011**, *10*, No. M111.007690.

https://doi.org/10.1021/acs.jproteome.2c00825
J. Proteome Res. 2023, 22, 977−989

(25) Teo, G.; Liu, G.; Zhang, J.; Nesvizhskii, A. I.; Gingras, A.-C.; Choi, H. SAINTexpress: Improvements and Additional Features in Significance Analysis of INTeractome Software. *J. Proteomics* **2014**, *100*, 37−43.
(26) Knight, J. D. R.; Choi, H.; Gupta, G. D.; Pelletier, L.; Raught, B.; Nesvizhskii, A. I.; Gingras, A.-C. ProHits-Viz: A Suite of Web Tools for Visualizing Interaction Proteomics Data. *Nat. Methods* **2017**, *14*, 645−646.
(27) Reimand, J.; Arak, T.; Adler, P.; Kolberg, L.; Reisberg, S.; Peterson, H.; Vilo, J. G:Profiler—a Web Server for Functional Interpretation of Gene Lists (2016 Update). *Nucleic Acids Res.* **2016**, *44*, W83−W89.
(28) Hulsen, T.; de Vlieg, J.; Alkema, W. BioVenn − a Web Application for the Comparison and Visualization of Biological Lists Using Area-Proportional Venn Diagrams. *BMC Genomics* **2008**, *9*, No. 488.
(29) Tyanova, S.; Temu, T.; Cox, J. The MaxQuant Computational Platform for Mass Spectrometry-Based Shotgun Proteomics. *Nat. Protoc.* **2016**, *11*, 2301−2319.
(30) Tyanova, S.; Temu, T.; Sinitcyn, P.; Carlson, A.; Hein, M. Y.; Geiger, T.; Mann, M.; Cox, J. The Perseus Computational Platform for Comprehensive Analysis of (Prote)Omics Data. *Nat. Methods* **2016**, *13*, 731−740.
(31) Rudolph, J. D.; Cox, J. A Network Module for the Perseus Software for Computational Proteomics Facilitates Proteome Interaction Graph Analysis. *J. Proteome Res.* **2019**, *18*, 2052−2064.
(32) Huttlin, E. L.; Bruckner, R. J.; Navarrete-Perea, J.; Cannon, J. R.; Baltier, K.; Gebreab, F.; Gygi, M. P.; Thornock, A.; Zarraga, G.; Tam, S.; Szpyt, J.; Gassaway, B. M.; Panov, A.; Parzen, H.; Fu, S.; Golbazi, A.; Maenpaa, E.; Stricker, K.; Guha Thakurta, S.; Zhang, T.; et al. Dual Proteome-Scale Networks Reveal Cell-Specific Remodeling of the Human Interactome. *Cell* **2021**, *184*, 3022.e28−3040.e28.
(33) Hein, M. Y.; Hubner, N. C.; Poser, I.; Cox, J.; Nagaraj, N.; Toyoda, Y.; Gak, I. A.; Weisswange, I.; Mansfeld, J.; Buchholz, F.; Hyman, A. A.; Mann, M. A Human Interactome in Three Quantitative Dimensions Organized by Stoichiometries and Abundances. *Cell* **2015**, *163*, 712−723.
(34) Cho, N. H.; Cheveralls, K. C.; Brunner, A.-D.; Kim, K.; Michaelis, A. C.; Raghavan, P.; Kobayashi, H.; Savy, L.; Li, J. Y.; Canaj, H.; Kim, J. Y. S.; Stewart, E. M.; Gnann, C.; McCarthy, F.; Cabrera, J. P.; Brunetti, R. M.; Chhun, B. B.; Dingle, G.; Hein, M. Y.; Huang, B.; et al. OpenCell: Endogenous Tagging for the Cartography of Human Cellular Organization. *Science* **2022**, *375*, No. eabi6983.
(35) Go, C. D.; Knight, J. D. R.; Rajasekharan, A.; Rathod, B.; Hesketh, G. G.; Abe, K. T.; Youn, J.-Y.; Samavarchi-Tehrani, P.; Zhang, H.; Zhu, L. Y.; Popiel, E.; Lambert, J.-P.; Coyaud, É.; Cheung, S. W. T.; Rajendran, D.; Wong, C. J.; Antonicka, H.; Pelletier, L.; Palazzo, A. F.; Shoubridge, E. A.; et al. A Proximity-Dependent Biotinylation Map of a Human Cell. *Nature* **2021**, *595*, 120−124.
(36) Pilot-Storck, F.; Chopin, E.; Rual, J.-F.; Baudot, A.; Dobrokhotov, P.; Robinson-Rechavi, M.; Brun, C.; Cusick, M. E.; Hill, D. E.; Schaeffer, L.; Vidal, M.; Goillot, E. Interactome Mapping of the Phosphatidylinositol 3-Kinase-Mammalian Target of Rapamycin Pathway Identifies Deformed Epidermal Autoregulatory Factor-1 as a New Glycogen Synthase Kinase-3 Interactor. *Mol. Cell. Proteomics* **2010**, *9*, 1578−1593.
(37) Dunham, W. H.; Larsen, B.; Tate, S.; Badillo, B. G.; Goudreault, M.; Tehami, Y.; Kislinger, T.; Gingras, A.-C. A Cost-Benefit Analysis of Multidimensional Fractionation of Affinity Purification-Mass Spectrometry Samples. *Proteomics* **2011**, *11*, 2603−2612.
(38) Rim, E. Y.; Clevers, H.; Nusse, R. The Wnt Pathway: From Signaling Mechanisms to Synthetic Modulators. *Annu. Rev. Biochem.* **2022**, *91*, 571.
(39) Stark, C. BioGRID: A General Repository for Interaction Datasets. *Nucleic Acids Res.* **2006**, *34*, D535−D539.
(40) Oughtred, R.; Rust, J.; Chang, C.; Breitkreutz, B.; Stark, C.; Willems, A.; Boucher, L.; Leung, G.; Kolas, N.; Zhang, F.; Dolma, S.; Coulombe-Huntington, J.; Chatr-aryamontri, A.; Dolinski, K.; Tyers, M. The BioGRID Database: A Comprehensive Biomedical Resource of Curated Protein, Genetic, and Chemical Interactions. *Protein Sci.* **2021**, *30*, 187−200.
(41) Alonso-López, D.; Gutiérrez, M. A.; Lopes, K. P.; Prieto, C.; Santamaría, R.; De Las Rivas, J. APID Interactomes: Providing Proteome-Based Interactomes with Controlled Quality for Multiple Species and Derived Networks. *Nucleic Acids Res.* **2016**, *44*, W529−W535.
(42) Alonso-López, D.; Campos-Laborie, F. J.; Gutiérrez, M. A.; Lambourne, L.; Calderwood, M. A.; Vidal, M.; De Las Rivas, J. APID Database: Redefining Protein−Protein Interaction Experimental Evidences and Binary Interactomes. *Database* **2019**, *2019*, No. baz005.
(43) Gingras, A. C.; Abe, K. T.; Raught, B. Getting to Know the Neighborhood: Using Proximity-Dependent Biotinylation to Characterize Protein Complexes and Map Organelles. *Curr. Opin. Chem. Biol.* **2019**, *48*, 44−54.
(44) Liu, X.; Salokas, K.; Tamene, F.; Jiu, Y.; Weldatsadik, R. G.; Öhman, T.; Varjosalo, M. An AP-MS- and BioID-Compatible MAC-Tag Enables Comprehensive Mapping of Protein Interactions and Subcellular Localizations. *Nat. Commun.* **2018**, *9*, No. 1188.
(45) Cox, J.; Hein, M. Y.; Luber, C. A.; Paron, I.; Nagaraj, N.; Mann, M. Accurate Proteome-Wide Label-Free Quantification by Delayed Normalization and Maximal Peptide Ratio Extraction, Termed MaxLFQ. *Mol. Cell. Proteomics* **2014**, *13*, 2513−2526.
(46) Kobayashi, T.; Hino, S.; Oue, N.; Asahara, T.; Zollo, M.; Yasui, W.; Kikuchi, A. Glycogen Synthase Kinase 3 and H-Prune Regulate Cell Migration by Modulating Focal Adhesions. *Mol. Cell. Biol.* **2006**, *26*, 898−911.
(47) Freitas, M. J.; Silva, J. V.; Brothag, C.; Regadas-Correia, B.; Fardilha, M.; Vijayaraghavan, S. Isoform-Specific GSK3A Activity Is Negatively Correlated with Human Sperm Motility. *MHR: Basic Sci. Reprod. Med.* **2019**, *25*, 171−183.
(48) Aizer, A.; Kafri, P.; Kalo, A.; Shav-Tal, Y. The P Body Protein Dcp1a Is Hyper-Phosphorylated during Mitosis. *PLoS One* **2013**, *8*, No. e49783.
(49) Rzeczkowski, K.; Beuerlein, K.; Müller, H.; Dittrich-Breiholz, O.; Schneider, H.; Kettner-Buhrow, D.; Holtmann, H.; Kracht, M. C-Jun N-Terminal Kinase Phosphorylates DCP1a to Control Formation of P Bodies. *J. Cell Biol.* **2011**, *194*, 581−596.
(50) Chiang, P.-Y.; Shen, Y.-F.; Su, Y.-L.; Kao, C.-H.; Lin, N.-Y.; Hsu, P.-H.; Tsai, M.-D.; Wang, S.-C.; Chang, G.-D.; Lee, S.-C.; Chang, C.-J. Phosphorylation of MRNA Decapping Protein Dcp1a by the ERK Signaling Pathway during Early Differentiation of 3T3-L1 Preadipocytes. *PLoS One* **2013**, *8*, No. e61697.
(51) Zhu, M.; Settele, F.; Kotak, S.; Sanchez-Pulido, L.; Ehret, L.; Ponting, C. P.; Gönczy, P.; Hoffmann, I. MISP Is a Novel Plk1 Substrate Required for Proper Spindle Orientation and Mitotic Progression. *J. Cell Biol.* **2013**, *200*, 773−787.
(52) Yamazaki, H.; Kosako, H.; Yoshimura, S. H. Quantitative Proteomics Indicate a Strong Correlation of Mitotic Phospho-/Dephosphorylation with Non-Structured Regions of Substrates. *Biochim. Biophys. Acta, Proteins Proteomics* **2020**, *1868*, No. 140295.
(53) Maarof, N. D.; Kumeta, M.; Yoshimura, S. H. Modulation of Actin-Binding and -Bundling Activities of MISP/Caprice by Multiple Phosphorylation. *Biochem. Biophys. Res. Commun.* **2021**, *561*, 128−135.
(54) Gupta, G. D.; Coyaud, É.; Gonçalves, J.; Mojarad, B. A.; Liu, Y.; Wu, Q.; Gheiratmand, L.; Comartin, D.; Tkach, J. M.; Cheung, S. W. T.; Bashkurov, M.; Hasegan, M.; Knight, J. D.; Lin, Z.-Y.; Schueler, M.; Hildebrandt, F.; Moffat, J.; Gingras, A.-C.; Raught, B.; Pelletier, L. A Dynamic Protein Interaction Landscape of the Human Centrosome-Cilium Interface. *Cell* **2015**, *163*, 1484−1499.
(55) Youn, J.-Y.; Dunham, W. H.; Hong, S. J.; Knight, J. D. R.; Bashkurov, M.; Chen, G. I.; Bagci, H.; Rathod, B.; MacLeod, G.; Eng, S. W. M.; Angers, S.; Morris, Q.; Fabian, M.; Côté, J.-F.; Gingras, A.-C. High-Density Proximity Mapping Reveals the Subcellular Organization of MRNA-Associated Granules and Bodies. *Mol. Cell* **2018**, *69*, 517.e11−532.e11.

https://doi.org/10.1021/acs.jproteome.2c00825
J. Proteome Res. 2023, 22, 977−989

(56) Hesketh, G. G.; Papazotos, F.; Pawling, J.; Rajendran, D.; Knight, J. D. R.; Martinez, S.; Taipale, M.; Schramek, D.; Dennis, J. W.; Gingras, A.-C. The GATOR−Rag GTPase Pathway Inhibits MTORC1 Activation by Lysosome-Derived Amino Acids. *Science* **2020**, *370*, 351−356.
(57) Dembowy, J.; Adissu, H. A.; Liu, J. C.; Zacksenhaus, E.; Woodgett, J. R. Effect of Glycogen Synthase Kinase-3 Inactivation on Mouse Mammary Gland Development and Oncogenesis. *Oncogene* **2015**, *34*, 3514−3526.
(58) Tanji, C.; Yamamoto, H.; Yorioka, N.; Kohno, N.; Kikuchi, K.; Kikuchi, A. A-Kinase Anchoring Protein AKAP220 Binds to Glycogen Synthase Kinase-3β (GSK-3β) and Mediates Protein Kinase A-Dependent Inhibition of GSK-3β. *J. Biol. Chem.* **2002**, *277*, 36955−36961.
(59) Reinton, N.; Collas, P.; Haugen, T. B.; Skålhegg, B. S.; Hansson, V.; Jahnsen, T.; Taskén, K. Localization of a Novel Human A-Kinase-Anchoring Protein, hAKAP220, during Spermatogenesis. *Dev. Biol.* **2000**, *223*, 194−204.
(60) Ruel, L.; Pantesco, V.; Lutz, Y.; Simpson, P.; Bourouis, M. Functional Significance of a Family of Protein Kinases Encoded at the Shaggy Locus in Drosophila. *EMBO J.* **1993**, *12*, 1657−1669.
(61) Korona, D.; Nightingale, D.; Fabre, B.; Nelson, M.; Fischer, B.; Johnson, G.; Lees, J.; Hubbard, S.; Lilley, K.; Russell, S. Characterisation of Protein Isoforms Encoded by the Drosophila Glycogen Synthase Kinase 3 Gene Shaggy. *PLoS One* **2020**, *15*, No. e0236679.

https://doi.org/10.1021/acs.jproteome.2c00825
J. Proteome Res. 2023, 22, 977−989